Pergamon

Int. J. Heat Mass Transfer. Vol. 39, No. 5, pp. 975–993, 1996
Copyright © 1995 Elsevier Science Ltd
Printed in Great Britain. All rights reserved
0017-9310/96 $15.00+0.00

0017-9310(95)00186-7

Numerical and experimental investigation of direct electric conduction in a channel flow

A. OULD EL MOCTAR, H. PEERHOSSAINI and J. P. BARDON†

Thermofluids and Complex Flows Research Group, Laboratoire de Thermocinétique de l'ISITEM,
Rue Christian Pauc, La Chantrerie, C.P. 3023, F-44087 Nantes Cedex 03, France

(*Received* 2 *December* 1994 *and in final form* 15 *May* 1995)

Abstract—Heat generation by direct electric conduction in a fully developed channel flow was studied to clarify interaction between the hydrodynamic, electric and thermal phenomena involved. The equations governing the system were solved numerically by a finite volume code. It was found that the difference between the residence time of the fluid flowing close to the wall and in the center of the channel causes deformation of the velocity profiles. This phenomenon creates a competition between the fluid particles flowing in these two regions and results in equalizing the temperature and velocity distribution in the channel span. An experimental investigation carried out in parallel with the numerical study yielded good agreement. An array of longitudinal streaks found on the channel electrode wall, with LIF visualization, is attributed to an instability phenomenon caused by electric body force. The wavelength of the streaks was measured and the control parameters of the instability were determined.

1. INTRODUCTION

Volume heating of liquids that contain free ions by direct electric conduction, or "ohmic heating", uses the electrical resistance of the liquid in order to heat it. In this process the liquid passes between two electrodes across which an a.c. potential difference is maintained, and heat is generated within the fluid by the Joule effect. The electrical resistance of the liquid is used to heat it directly through its volume, and thus, the temperature distribution within the liquid is uniform. The method therefore has the advantage of being able to handle fluids that are heat-sensitive, or have high viscosity and/or low thermal conductivity, on the condition that they contain free ions. This process also obviates the problems linked to heating by a hot surface and so is a valuable alternative to conventional heating methods such as tubular and plate heat exchangers, etc. Furthermore, ohmic heating is a very flexible technique, so that it can be used with a regulation system to control the flow of energy or to maintain constant temperature in order to attain a desired rate of temperature increase.

Attempts to apply this method, which has been known since the end of the last century, have mainly been focused in the food industry, where the speed and uniformity of heating is attractive for operations such as defrosting, sterilization, bleaching, cooking, etc. [1]. In this field, one of the greatest successes is the 'ohmic heater' [2] for processing products containing solid pieces. Ohmic heating is perfectly suited to this type of liquid; in some circumstances the temperature at the heart of the solid piece can be raised above that in the liquid. This is almost impossible to achieve with conventional heating methods. In other areas of industry, the best known application of the principle is the use of electrode boilers to produce steam or hot water.

Most previous work has concentrated on the technological aspects of direct electric conduction (DEC) and on adapting the system to existing processes, and therefore, has neglected the physical phenomena occurring in these heaters. The simplicity of the principle behind this heating method should not be allowed to mask the variety and complexity of the physical phenomena (hydrodynamic, thermal, electrical and electrochemical) that come into play, or the strong couplings among them.

The process of volume heating by direct electric conduction is generally classified as being in the field of electrohydrodynamics coupled with heat transfer [3] or 'thermoelectrohydrodynamics' (TEHD), a subject that has been the focus of intensive research since the 1930s [4]. Those investigations were mostly oriented towards applications in traditional heat exchangers with the specific purpose of developing new liquids which could be used in heat exchangers. They thus concerned the increase of the heat transfer coefficient on a heated surface caused by the application of an electric field, and also often involved an electrically insulating liquid. However, these studies provided an opportunity to characterize the coupling between electric and thermal fields in various situations. The same configurations were also used to study the coupling between the electric and hydrodynamic fields via the highly interesting phenomenon of electroconvective instability [5].

---

† Interface and Microscale Heat Transfer Research Group.

NOMENCLATURE

a	mean thermal diffusivity of fluid [$\mathrm{m^2\ s^{-1}}$]
Br	Brinkman number
c_p	constant pressure specific heat [$\mathrm{J\ kg^{-1}\ K^{-1}}$]
D/Dt	total derivative
$\vec{E}$	electric field [$\mathrm{V\ m^{-1}}$]
E_1, E_1', E_1''	electric Grashof numbers
f	frequency [Hz]
$\vec{f}_e$	electric force [N]
$\vec{g}$	gravitation acceleration [$\mathrm{m\ s^{-2}}$]
Gr	Grashof number
H	electrode length [m]
I	current intensity [A]
$\vec{J}$	current density [$\mathrm{A\ m^{-2}}$]
l	inter-electrode distance [m]
p	pressure [Pa]
P_c	thermal power [W]
P_{el}	electric power [W]
Ra	Rayleigh number
Re	Reynolds number
Ri	Richardson number
t	time [s]
T	temperature [K]
T_{in}	temperature at the entrance to the channel [K]
T_{out}	temperature at the channel exit section [K]

T_0	reference mean temperature [K]
T^*	nondimensional temperature
u	spanwise velocity component [$\mathrm{m\ s^{-1}}$]
U	electric potential [V]
U_0	potential difference [V]
v	streamwise velocity component [$\mathrm{m\ s^{-1}}$]
$\vec{V}$	velocity vector [$\mathrm{m\ s^{-1}}$]
V_m	mean streamwise velocity [$\mathrm{m\ s^{-1}}$]
V_{axe}	ascending velocity on the cell axis [$\mathrm{m\ s^{-1}}$].

Greek symbols

Δ	Laplacian operator
ΔT_{wc}	temperature difference between wall and center [K]
ε	electric permittivity [$\mathrm{C\ V^{-1}\ m^{-1}}$]
ϕ_{el}	electric source term [$\mathrm{K\ s^{-1}}$]
λ	thermal conductivity [$\mathrm{W\ m^{-1}\ K^{-1}}$]
μ	viscosity [$\mathrm{kg\ m^{-1}\ s^{-1}}$]
ν	kinematic viscosity [$\mathrm{m^2\ s^{-1}}$]
ρ	specific mass [$\mathrm{kg\ m^{-3}}$]
ρ_e	free charge density [$\mathrm{C\ m^{-3}}$]
σ	electric conductivity [$\mathrm{S\ m^{-1}}$]
$\bar{\bar{\tau}}$	viscous stress tensor
τ_σ	relaxation time [s]
$\vec{\nabla}$	gradient
$\nabla .$	divergence
$\nabla \times$	curl.

In spite of significant effort in investigating the technical and the fundamental aspects of this heating method, however, there has so far been little interaction between them, and this lack has prevented a more efficient use of volume heating technique with all the advantages it offers. This work, therefore, attempts to give a more global view of the problem by modeling and analyzing the various physical phenomena arising in this type of heating, looking in particular at volume heating of an ionic liquid in a fully developed channel flow by direct electric conduction.

In Section 2 we establish the equations that govern the system and underline the coupling between the various physical phenomena. The system of equations is then resolved in Section 3 using a finite volume computer code "ULYSSE". In Section 4 we describe an experimental apparatus constructed to validate the above model. Various experimental methods are used: laser Doppler anemometry for the measurement of velocity profiles, electrically isolated thermocouple probes, and flow visualization by laser-induced fluorescence (LIF) technique. Experimental validation of the numerical model is treated in Section 5.

2. PHYSICAL ANALYSIS AND GOVERNING EQUATIONS

The heating of a flowing ionic liquid by an electric power density brings into play a variety of phenomena: hydrodynamic, thermal, electrical and electrochemical. However, under certain conditions (50 Hz a.c., low current density, good choice of electrode–liquid pair), electrochemical reactions at the electrode–liquid interface can be ignored [6].

The equations which govern the system take into consideration the following physical aspects [3]:

(1) The hydrodynamic aspect, including the equation of continuity and the equations of motion (Navier–Stokes equation) containing force terms due to the gravitational field, the pressure field, internal friction and especially to electric force.

(2) Heat transfer by conduction and convection. The existence of a temperature gradient may result in natural convection that is superposed on the forced convection and we then have a mixed convection regime. The equation of conservation of energy will contain electrical and viscous dissipation terms.

(3) The electrical phenomenon that causes heating

of the liquid by the volume dissipation of electric energy (the Joule effect). The electrical equations must take into account Gauss's theorem, the field rotation equation and the equation of conservation of electricity.

The equations will then be solved numerically for the case of an ionic liquid and for two-dimensional (2D) geometry, that is a fully developed channel flow.

2.1. *Hydrodynamic equations*

The equation of continuity for an incompressible fluid is

$$\nabla . \vec{V} = 0. \tag{1}$$

The equation of conservation of momentum for an incompressible viscous fluid, with an additional term for the electric force ($\vec{f}_e$) which represents the response of the fluid to the electric field, is

$$\rho \frac{D\vec{V}}{Dt} = -\vec{\nabla} p - \rho \vec{g} + \vec{f}_e + \nabla . \bar{\bar{\tau}} \tag{2}$$

where

$$\bar{\bar{\tau}} = \mu\left(\frac{\partial V_i}{\partial x_j} + \frac{\partial V_j}{\partial x_i}\right). \tag{3}$$

The electric force acting on the liquid is expressed as [3]

$$\vec{f}_e = \rho_e \vec{E} - \tfrac{1}{2} E^2 \vec{\nabla}\varepsilon - \vec{\nabla}\left(\tfrac{1}{2}\rho E^2 \left(\frac{\partial\varepsilon}{\partial\rho}\right)_T\right). \tag{4}$$

2.2. *Energy equation*

Taking into account the terms for electrical and viscous dissipation, the equation of conservation of energy can be written as:

$$\rho c_p \frac{DT}{Dt} = \nabla .(\lambda \vec{\nabla} T) + \sigma E^2 + \bar{\bar{\tau}} : \bar{\bar{\nabla}} \vec{V}. \tag{5}$$

2.3. *Electrical equations*

For a linear ohmic dielectric medium, the electrostatic equations are

$$\nabla .(\varepsilon \vec{E}) = \rho_e \tag{6}$$

$$\nabla \times \vec{E} = 0 \tag{7}$$

$$\nabla . \vec{J} + \frac{\partial \rho_e}{\partial t} = 0 \tag{8}$$

where

$$\vec{J} = \rho_e \vec{V} + \sigma \vec{E} \tag{9}$$

is the current density. The hydrodynamic, thermal and electrical phenomena interact; as represented schematically in Fig. 1 (the arrows represent the direction of the interaction). A more detailed account of the governing equations can be found in [7]. The nature and the importance of the couplings between the various physical phenomena must be analyzed before making any simplifying hypotheses.

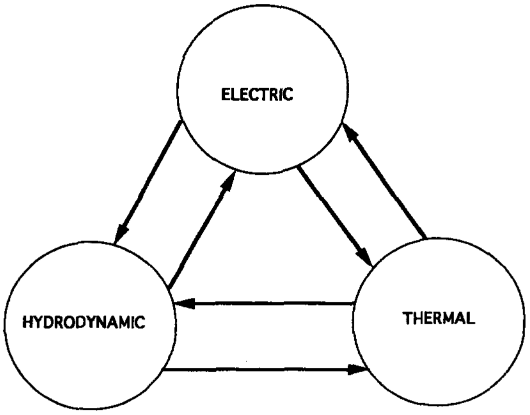

Fig. 1. Physical phenomena involved in direct electric conduction heating.

2.4. *Electrical–thermal coupling*

In the electrical-to-thermal direction, the electrical energy density (σE^2) dissipated by the Joule effect (ohmic conduction) acts directly on the temperature field T and constitutes one of the main couplings. Discontinuity or concentration of electric current lines caused by electrodes geometry generally results in a local increase in the current density. This high current density causes local overheating and the appearance of temperature gradients that modify the electrical $\sigma(T)$ and thermal $\lambda(T)$ conductivities as well as the dissipated electrical power density.

2.5. *Electrical–hydrodynamic coupling*

The direct interaction between electrical and hydrodynamic phenomena can be linked to the thermal field and appear when there is a non-zero electric force density ($\vec{f}_e \neq 0$) or a non-zero charge density ($\rho_e \neq 0$). The existence of temperature gradients can give rise to a net electric force density that modifies the flow. In the most general case, this electric force density $\vec{f}_e$, made up of three terms, is given by equation (4). The last term can be neglected in the case of an incompressible fluid. The importance of the first two terms depends on the ratio $\tau_\sigma = \varepsilon/\sigma$, that is, the relaxation time for free charges. Two cases can occur:

(1) If the frequency f of the alternating field is such that $f \gg 1/\tau_\sigma$, then no free electric charge can appear in the volume or at the boundary and the first term $\rho_e E$ is zero. Only the second term remains, which is linked to a permittivity gradient. If ε depends strongly on the temperature, then

$$\vec{\nabla}\varepsilon = \left(\frac{\partial \varepsilon}{\partial T}\right)\vec{\nabla}T \qquad (10)$$

is not negligible and an electric force density

$$\vec{f}_{\mathrm{e}} = -\tfrac{1}{2}E^2\left(\frac{\partial \varepsilon}{\partial T}\right)\vec{\nabla}T \qquad (11)$$

exists. In this case, and for more insulating liquids, a regime of electroconvection can appear under the action of the electric force $\vec{f}_{\mathrm{e}}$. This phenomenon is similar to the natural convection, with the difference that the buoyancy force is replaced by electric force. Ashmann and Kronig [8] have characterized this regime and its corresponding heat transfer enhancement by an 'electric Grashof' number:

$$E_{\mathrm{l}} = E^2\left(\frac{\partial \varepsilon}{\partial T}\right)\frac{\Delta T_{\mathrm{ref}}l^2}{\rho \nu^2} \qquad (12)$$

where ΔT_{ref} is the reference temperature deviation and l is a characteristic length.

(2) If $f \ll 1/\tau_\sigma$, for conducting liquids, the electrical conductivity gradient causes the accumulation of free charges in the volume, and it is the term ρ_{e} which dominates. The electric force density $\vec{f}_{\mathrm{e}}$ which reduces to $\rho_{\mathrm{e}}\vec{E}$ and depends on the electrical conductivity gradient σ (as we shall see later), can modify the flow. A regime of electroconvection sets in and can be characterized by another 'electric Grashof' number E'_{l}. An expression for this number is proposed by Bonjour and Verdier [9]:

$$E'_{\mathrm{l}} = E^2(3a+2b)\varepsilon_0\frac{\Delta T_{\mathrm{ref}}l^2}{\rho \nu^2} \qquad (13)$$

where a and b represent the temperature coefficients of the linearized laws

$$\sigma(T) = \sigma_0(1-b(T-T_0)), \quad \varepsilon(T) = \varepsilon_0(1+a(T-T_0)).$$

Depending on the size of the nondimensional numbers E_{l} and E'_{l}, the electroconvective coupling effects can be either significant or negligible.

In addition, in the hydrodynamic-to-electric direction, the existence of free charges ($\rho_{\mathrm{e}} \neq 0$) modifies the current density by a transport term linked to the velocity $\vec{V}$ according to equation (9).

2.6. *Hydrodynamic–thermal coupling*

In the hydrodynamic-to-thermal direction, the fluid particles are slowed down by viscosity in the vicinity of the walls (hydrodynamic boundary layers) and, therefore, their residence time in the electric field is longer than those situated in the core flow. The result is excess local heating of the fluid particles and thus of the electrode walls. So that a temperature gradient appears across the flow in the direction normal to the wall.

A second phenomenon that must be taken into account for very viscous fluids is the energy dissipated by internal friction, or viscous dissipation, which can contribute significantly to heating. The Brinkmann number (*Br*) characterizing this effect is defined as the ratio of mechanical power dissipated by viscosity to the heat transferred. If *Br* is very small compared to 1, the viscous dissipation term can be ignored. The thermal field is thus coupled to the flow field by viscous dissipation and to the electric field by the Joule effect.

Another coupling effect in the thermal-to-hydrodynamic direction is the influence of heating (the Joule effect) on the viscosity and therefore on the flow. Most fluids, whether Newtonian (characterized by a viscosity μ) or non-Newtonian (characterized by an apparent viscosity μ_{a}), have a viscosity that depends on the temperature and often follows a relationship of the type $\mu = A\,.\,\mathrm{e}^{\mathrm{B}/\mathrm{T}}$, with T in degrees Kelvin. The flow regime and instability threshold can be modified considerably by this dependence on temperature.

The temperature gradient across the flow can also give rise to natural convection which is superposed on the base flow and results in a mixed convection regime. The Richardson number $Ri = Gr/Re^2$, defined as the ratio between the Grashof number and the square of the Reynolds number, measures the relative importance of free convection with respect to the forced convection.

3. NUMERICAL STUDY

Given the complexity of the various couplings between the phenomena involved and the nonlinearities of the equations, the problem is solved for a simple geometry that also corresponds to the technological applications: a rectangular duct flow of aspect ratio 5 whose two larger opposing walls are electrodes. Therefore, the phenomena can be considered quasi-two-dimensional. The only spatial variables entering into the equations are the x-axis in the direction perpendicular to the electrodes and the y-axis in the main flow direction.

We therefore consider a vertical channel flow in which the equations (1)–(9) can be simplified by the following assumptions:

(1) The flow is a fully developed channel flow with two electrode walls, and two dimensional.

(2) The working fluid is a conducting ionic incompressible fluid for which the three terms of the electric force $\vec{f}_{\mathrm{e}}$ are assumed negligible. The effect of this force appears in the direction normal to the flow plane and therefore this assumption is justified.

(3) The velocities are small and the viscous dissipation term is assumed negligible.

(4) The physical properties λ, μ and σ depend only on the temperature T. The density ρ is considered constant except in the buoyancy term in the equations of motion (2) (Boussinesq approximation).

(5) Fluid enters the channel at constant temperature T_{in}.

With the above assumptions the system to be solved can be written as follows:

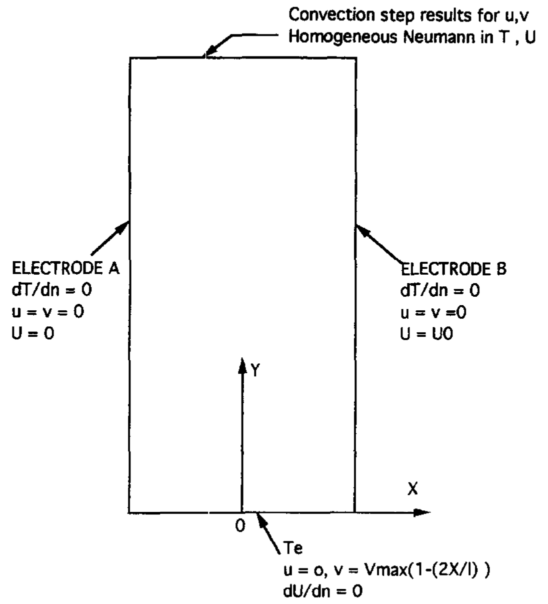

Fig. 2. Boundary conditions for numerical model.

$$\begin{aligned} &\nabla . \vec{V} = 0 \\ &\rho \frac{\mathrm{D}\vec{V}}{\mathrm{D}t} = -\vec{\nabla} p - \rho \vec{g} + \nabla . (\mu(T) \nabla \vec{V}) \\ &\rho c_{\mathrm{p}} \frac{\mathrm{D}T}{\mathrm{D}t} = \nabla . (\lambda(T) \vec{\nabla} T) + \sigma(T) (\vec{\nabla} U)^2 \\ &\nabla . (-\sigma(T) \vec{\nabla} U) = 0 \end{aligned} \tag{14}$$

where U is electric potential.

The boundary conditions corresponding to the case under consideration here are summarized in Fig. 2. and are detailed in Section 3.1. They are hydrodynamic, thermal and electrical boundary conditions.

3.1. *Numerical method*

The system of equations (14) consists of hydrodynamic equations (Navier–Stokes), the equation of conservation of energy and an electrical equation. We have used a finite volume code ULYSSE, developed by the Laboratoire National d'Hydraulique of EDF to solve it.

The equations to be solved have three types of terms: convection or transport terms, diffusion terms, and pressure terms. For optimal numerical resolution of the equations, ULYSSE uses the technique of 'composed steps' [10], which entails breaking the problem in several substeps so that the solvers best suited to the properties of each substep can be used. To give an idea of how this method works, we apply it to the Navier–Stokes equations.

If the derivative with respect to time is approximated by a first-order finite difference

$$\frac{\partial \vec{V}}{\partial t} = \frac{\vec{V}^{n+1} - \vec{V}^{n}}{\mathrm{d}t} \tag{15}$$

the scheme for calculating velocity $\vec{V}^{n+1}$ at time t_{n+1} from the known velocity $\vec{V}^{n}$ at time t_n is expressed, to the first order in time, as

$$\vec{V}' - \vec{V}^{n} = -\vec{V} . \nabla \vec{V} . \mathrm{d}t \quad \text{(convection step)} \tag{16}$$

$$\vec{V}'' - \vec{V}' = \nabla . \left(\frac{\mu}{\rho} \nabla \vec{V}'' \right) . \mathrm{d}t \quad \text{(diffusion step)} \tag{17}$$

$$\vec{V}^{n+1} - \vec{V}'' = -\frac{1}{\rho} \vec{\nabla} p^{n+1} . \mathrm{d}t. \quad \text{(pressure step)}. \tag{18}$$

By adding the three steps together we obtain the general equation

$$\frac{\vec{V}^{n+1} - \vec{V}^{n}}{\mathrm{d}t} + \vec{V}^{n} \nabla \vec{V} - \nabla . \left(\frac{\mu}{\rho} \nabla \vec{V}'' \right) + \frac{1}{\rho} \vec{\nabla} p^{n+1} = 0. \tag{19}$$

Step I [equation (16)], called the 'convection step', is written in another form via a domain transformation and is solved by the method of characteristics. This method is also used to resolve the transport terms of the energy equation. Step II [equation (17)], the 'diffusion step', is solved by the method of conjugate residuals. Step III [equation (18)], the 'pressure step', combined with the equation of continuity ($\nabla . \vec{V}^{n+1} = 0$), gives a Laplacian pressure equation, which is resolved by the method of conjugate residuals. The same method is used to solve the diffusion term in the energy equation and in the electrical equation.

In its standard form, the code handles only fluid mechanics equations. A subprogram (DIFFTP) solves the diffusion term of the energy equation in the form

$$\frac{T^{n+1} - T'}{\mathrm{d}t} = \nabla . (a \vec{\nabla} T^{n+1}) + \Phi_{\mathrm{el}}, \tag{20}$$

where Φ_{el} represents the electric density source term, which we have added to compute the thermal field as a function of the distribution of electrical potential and of the electrical conductivity of the liquid to be heated. In equation (20) a is the thermal diffusivity.

In order to resolve the electrical equation, a specific subprogram (POTENT) has been developed which is identical in form to the thermal subprogram but lacks the source and transient terms. POTENT thus solves the equations of the type

$$\nabla . (\sigma \vec{\nabla} U) = 0 \tag{21}$$

where σ is the electrical conductivity of the liquid.

3.2. *Boundary conditions*

3.2.1. *Hydrodynamic boundary conditions.* These consist of: a non-slip, non-penetration condition on the walls: $u = v = 0$; a condition of an imposed velocity profile at the input and the boundary condition at the output is given by the solution to the convection step (step I) and verification of the conservation of mass. More details on the implementation of this boundary condition are given in ref. [10].

3.2.2. *Thermal boundary conditions.* These consist of: uniform temperature T_{in} at the input to the flow field and thermal insulation condition $\partial T/\partial n = 0$ at the output and on all walls including the electrodes. The latter condition is not realistic, but if we consider that the electrodes are thin and backed by an insulating material, we can then ignore the heat transferred by conduction perpendicular to the electrodes and in the horizontal and vertical directions.

3.2.3. *Electrical boundary conditions.* These consist of: zero electric potential imposed on electrode A and electrode B maintained at potential U_0.

An electrical insulation condition is assumed on all other walls.

3.3. *Numerical results*

The system of equations (14) has been solved for water with thermophysical properties varying with temperature as

$$\rho(T) = 1007.5-0.435(T-273)$$

$$\mu(T) = (1791-52.215(T-273)+0.75048(T-273)^2 -4.0747\times 10^{-3}(T-273)^3)\times 10^{-6}$$

$$\lambda(T) = 0.5630+2.1747\times 10^{-3}(T-273) -1.216\times 10^{-5}(T-273)^2 +1.4933\times 10^{-8}(T-273)^3$$

$$\sigma(T) = 0.01023+6.8789\times 10^{-4}(T-273)$$

where T is the local temperature in degrees K.

The equations have been solved for water with average temperature increase $T_{\text{out}}-T_{\text{in}} = 10.46$ K starting from a uniform input temperature of 293 K. At this temperature the working fluid has the following average physical properties:

$$\rho_0 = 996.84\,\text{kg}\,\text{m}^{-3};$$

$$c_p = 4185\,\text{J}\,\text{kg}^{-1}\,\text{K}^{-1};$$

$$\mu_0 = 0.8843\times 10^{-3}\,\text{kg}\,\text{m}^{-1}\,\text{s}^{-1}$$

$$\lambda_0 = 0.61\,\text{W}\,\text{m}^{-1}\,\text{K}^{-1} \quad \text{and}$$

$$\sigma_0 = 2.75\times 10^{-2}\,\text{S}\,\text{m}^{-1}.$$

We have used as input, for computations, a velocity profile measured at the entrance to the test section of the experimental apparatus described in Section 4. The imposed velocity profile at input gives a mean velocity $V_{\text{m}} = 7.3$ mm s^{-1}, which requires the thermal power

$$P_{\text{c}} = \rho_0 c_{\text{p}} V_{\text{m}} l(T_{\text{out}}-T_{\text{in}}). \tag{22}$$

We also have

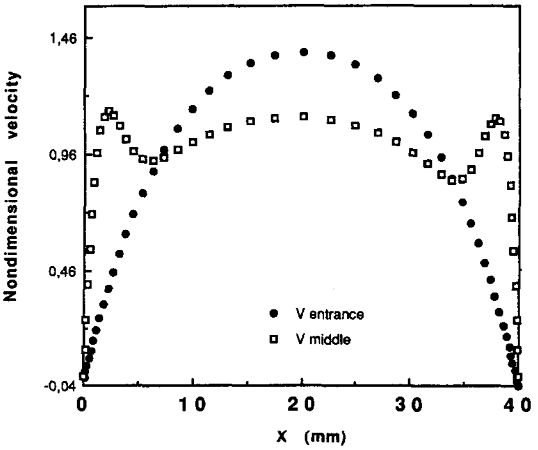

Fig. 3. Comparison between computed velocity profiles at entrance to and middle of test section.

$$P_{\text{c}} = P_{\text{el}} = \sigma_0 E^2 Hl = \frac{\sigma_0 U_0^2}{l^2}.Hl \tag{23}$$

so that

$$U_0^2 = \frac{\rho_0 c_{\text{p}} V_{\text{m}} l^2 (T_{\text{out}}-T_{\text{in}})}{\sigma_0 H} \tag{24}$$

which gives a value for electric potential $U_0 = 242.5$ volts.

Figure 3 shows velocity profiles at the entrance and the middle of the test section. Velocities are nondimensionalized with the mean velocity in the channel defined as

$$\int_{-l/2}^{l/2} \frac{u(x)\,\mathrm{d}x}{l}.$$

The flow velocity is much higher at the middle of the channel than in the vicinity of the walls. The particles passing in the vicinity of the walls remain longer under the influence of the electric field and are heated more than those traveling faster in the middle of the channel. This difference in residence time causes a temperature gradient between the center of the flow and the vicinity of the walls. The horizontal temperature gradient is added to the progressive heating of the liquid that takes place as it passes through the channel. The special form of the velocity profile in the channel mid-height can be explained by the effect of the horizontal temperature gradient. Fluid particles in the vicinity of the wall travel faster, in comparison to those on the input velocity profile, due to smaller density, and hence natural convection arises. Fluid particles in the channel center, on the contrary, move more slowly since they have not been under the effect of electric field as long as the particles close to the walls have been. This trend is reversed farther downstream, as discussed below.

The effect of the natural convection is an acceleration of the hot liquid in the vicinity of the wall; in other words, there is a noticeable decrease in the

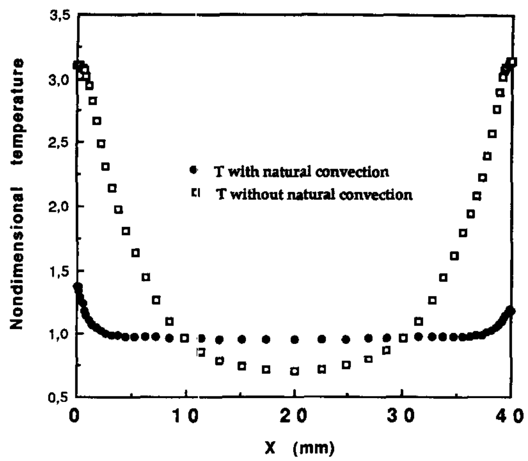

Fig. 4. Computed temperature profiles at exit from test section with and without free convection.

thickness of the boundary layer. A direct consequence of this acceleration is that the velocity becomes more uniform in any given section of the channel compared with the parabolic profile imposed at the input (Fig. 3). The temperature profile at the output of the channel also becomes more uniform. Figure 4 shows the temperature distribution in the channel span for the exit from the channel. Temperatures are non-dimensionalized as:

$$T^* = \frac{T_{\text{local}} - T_{\text{in}}}{T_{\text{out}} - T_{\text{in}}}. \tag{25}$$

The effect of natural convection on the temperature uniformity in the channel span is discernible.

There are other causes of flow acceleration close to the wall. If the electrodes do not completely cover the vertical wall, there is a discontinuity in the electric field at their edges. The electric current lines will thus converge, closing on themselves at the extremities of the electrodes, and this increases the electric current density at these points and becomes an additional cause of local overheating.

It should be noted that the electrical conductivity increases with temperature, and when either the conductivity or the current density increases, the power density and thus the temperature increase locally. For this reason thermohydraulic conditions in real heaters of this type must be optimized in order to avoid overheating and fouling.

The flow acceleration in the wall vicinity and flow deceleration in the channel center, both under the effect of the electric field, give a dynamical property to the flow. The consequence of this acceleration–deceleration downstream of the flow is a reverse effect that decelerates the accelerated particles and accelerates the decelerated fluid. This competition continues all the way to the channel exit. To show this scenario for a parabolic input velocity profile, we give in Fig. 5 the computed velocity distribution in the channel at 181, 346, 501 and 600 mm from the entrance to the channel. Velocity peaks and the valley at the channel center and velocity peaks close to the two walls oscillate around a mean as the flow travels downstream. The mean is the ideal uniform velocity that would obtain if the channel were infinitely long. The immediate effect of this spatial oscillation is the tendency towards a uniform velocity and consequently uniform temperature distribution. It should be mentioned that these results are obtained with the flow parameters different from the previous computations.

In order to capture the behavior of the spatial oscillation of velocity and its relation to temperature, we show in Fig. 6 the velocity at the channel center V_{ax}, vs the distance from the channel entrance. The same figure also shows the difference between the fluid temperature on the wall and in the channel center ΔT_{wc} against the same spatial variable. The velocity shows a wave-form oscillation with decaying amplitude: its maximum amplitude occurs at the entrance and it tends to a uniform velocity as it approaches the channel exit. The temperature difference ΔT_{wc} starts at a zero value, since the temperature input is uniform. Its evolution is out of phase with and always ahead of the velocity variation, showing that in fact the generation of a horizontal temperature gradient is the driving mechanism of the spatial velocity oscillations. As in the case of velocity, the amplitude of ΔT_{wc} decays in the downstream direction, leading to a uniform temperature distribution in the channel span. This self-regulating behavior of the temperature is of course of great importance for applications.

4. EXPERIMENTAL STUDY

An experimental apparatus was designed to study the heating of flowing ionic liquids by direct electric conduction. It is equipped with laser Doppler velocimeter (LDV) to measure the velocity field, thermocouple instrumentation to measure the temperature field; laser induced fluorescence (LIF) technique was used for visualization of the flow structures and instabilities caused by the geometry and the electric field. Below we give a brief description of the experimental installations and procedures; a detailed account of it is given in [11].

4.1. *Experimental apparatus and methods*

The experimental loop in Fig. 7 consists of a transparent Plexiglas test cell (4) comprising the following parts:

(1) a lower mixing tube filled with glass beads to form a porous medium; this serves to break down the central jet flow caused by the small diameter of the inlet pipe and the large angle of the upstream diffuser;

(2) a settling chamber, used to slow down the flow and make the perturbations decay;

(3) an intermediate mixing tube, to reduce the loop cross-section to the test section dimensions, (40 × 200 mm). This tube contains a series of screens that break

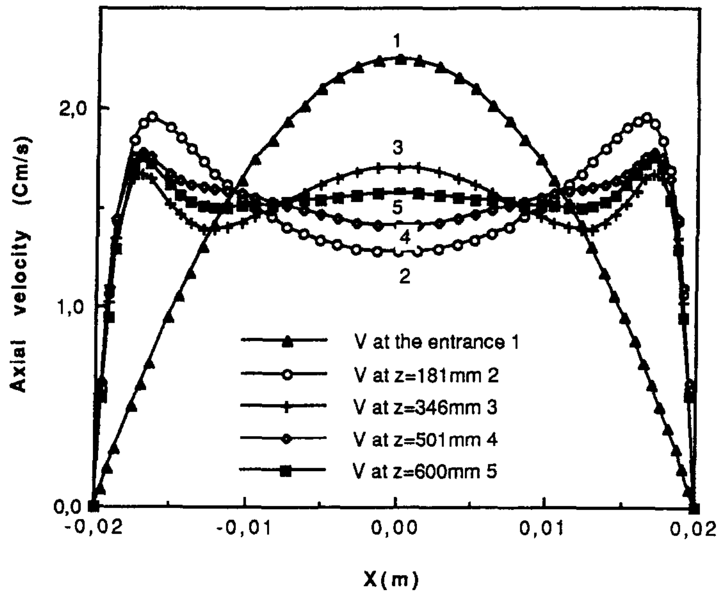

Fig. 5. Velocity profiles at different distances from entrance to test section.

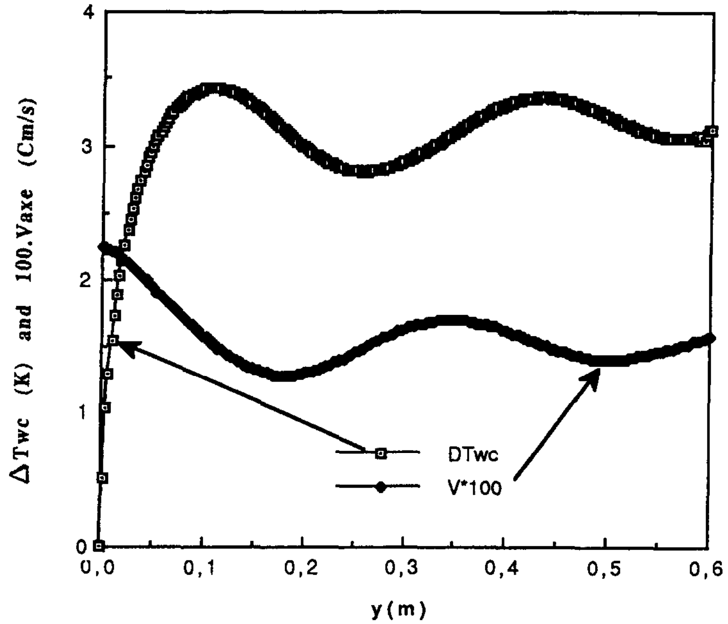

Fig. 6. Evolution of velocity in center of test section and temperature difference between wall and center of test section as a function of distance from entrance.

down any remaining large structures and even out the pressure distribution;

(4) the test section is a duct of 40 × 200-mm cross-section and 500-mm length. The two 40 × 500-mm walls are transparent, while the other two 200 × 500-mm walls are made of the metal constituting the electrodes. Each electrode has an H-shaped window for flow visualization or LDV measurement with vertical branches of height 10 mm. Upstream of the electrodes, two dye-injection channels inject tracer solution on the walls by transpiration through a porous metal bar and

(5) the exit nozzle brings the liquid from the test section to the output circuit.

The working liquid (water or non-Newtonian fluid) is stored in a tank (1) and driven by a pump (2). Flow rate is measured by an electromagnetic flowmeter (3) which measures the real mass flowrate independent from the variations of the thermophysical properties of the working fluid. The system can work in a closed or open loop. Except in the flow visualization tests, the system works in a closed loop. In this case the liquid must be cooled after passing through the test

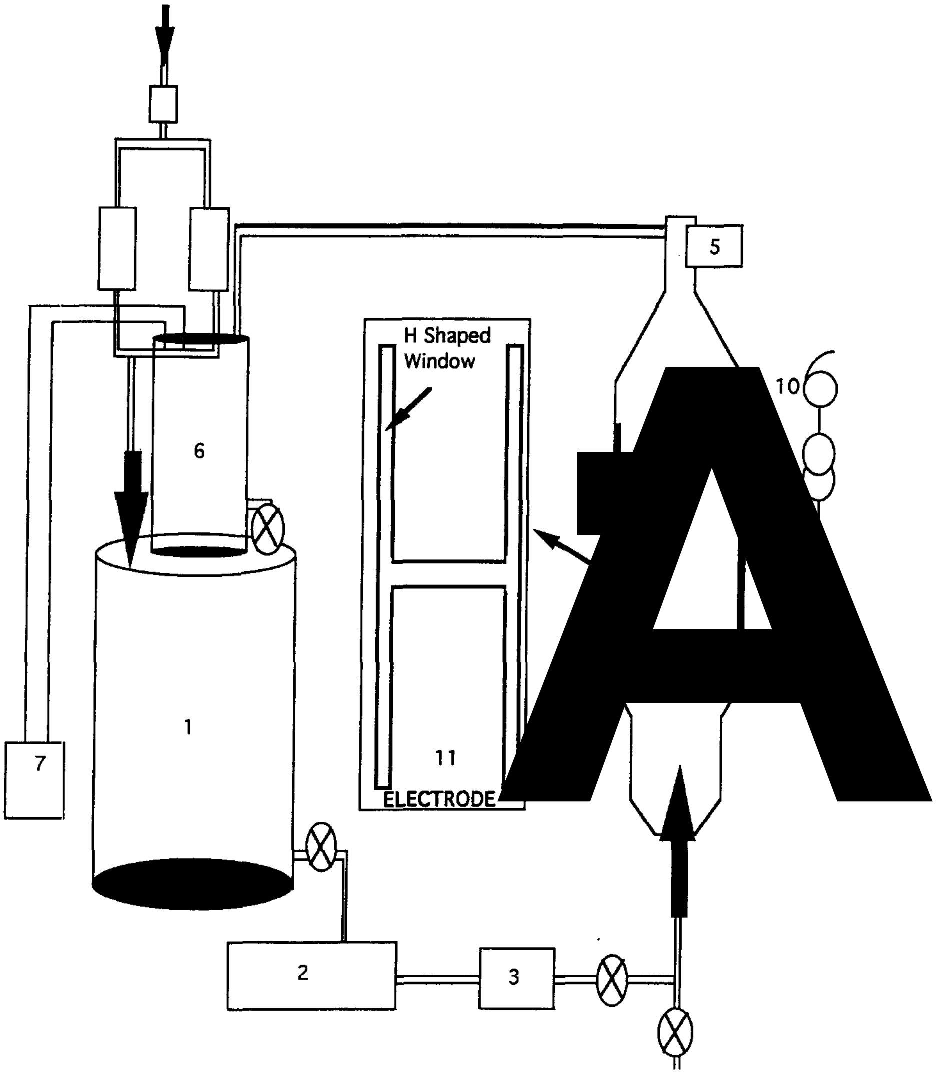

Fig. 7. Schematic diagram of experimental apparatus.

section, in order to maintain a constant input temperature. To do this, the fluid first goes into a primary tank (6) equipped with a coil. Water at a controlled temperature (Lauda RK20 (7)) circulates around the coil and cools the working liquid to the temperature of the liquid stored in the tank (1).

The electric power supply is 50 Hz a.c. single-phase. An auto transformer (10) connected to the mains provides a variable voltage adjustable from 0 to 220 volts. A transformer (9) then raises this voltage to supply a potential difference which can vary between 0 and 660 V. This potential difference is applied between the electrodes (11) by connecting the transformer output to the power supply terminals soldered to the electrodes. (The connections are made via a switchboard equipped with various protection devices.)

The experimental facility is equipped with several thermocouples for measuring the temperature. A constantan-copper thermocouple mobile probe of 1 mm bead, covered by a steel sheath and isolated by a dielectric material, is used to measure temperature profiles inside the test section under an electric field. Its precision is estimated to be 0.2 K in the range of measured temperatures. The thermocouple probe is bent so that the thermocouple wires are aligned with isothermal lines. A micrometric displacement mechanism provides the translation of the probe in the test section span. Since we are interested in the temperature profile at the exit from the test section, the thermocouple probe traverses the span at the exit plane of the apparatus. Other thermocouples are used to measure the average input and output temperatures of the working fluid.

Measurements were carried out for a flow rate of 150 l h^{-1} and an average input–output temperature difference of 10.5 K. For these working parameters, an average electric power of 1743 W at a voltage of 273 V is necessary. The electrical conductivity of water used in this experiment is 195 $\mu\Omega^{-1}$ cm^{-1} and the

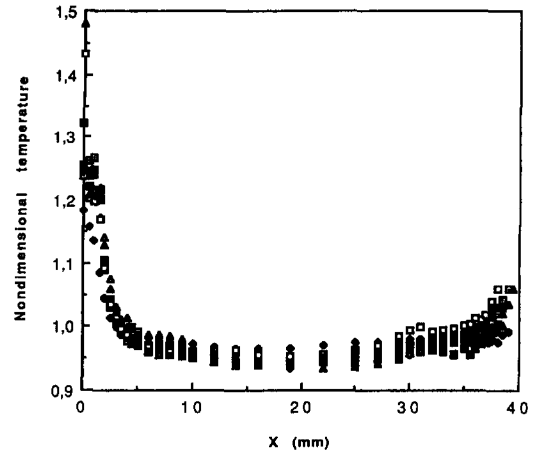

Fig. 8. Temperature profile at exit from test section for different sets of variable parameters.

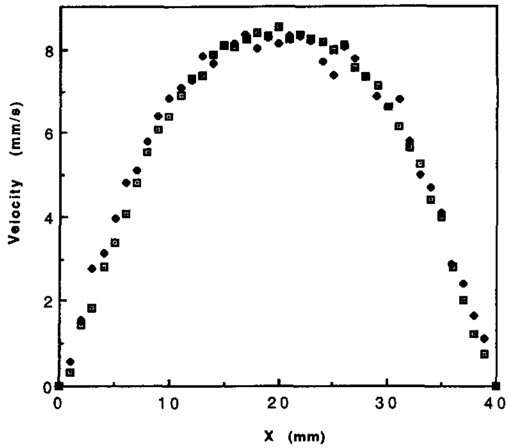

Fig. 9. Velocity profile at entrance to test section: experiment.

average current density sustained between two electrodes is 15.2 mA cm^{-2}.

A nondimensional temperature is defined with the input and output temperatures as described in (25). Figure 8 shows several dimensionless temperature profiles corresponding to different sets of experimental parameters measured at the end of electrode plates. The scatter of the results is 7%, showing that the above nondimensional temperature can universally represent the temperature distribution for different runs.

The asymmetry of the temperature on the test section walls should be noted. This is caused by the unequal lengths of the electrode plates: the right-hand electrode is 2 mm shorter than the left-hand electrode, and therefore the fluid particles on the right are exposed to the electric field for a shorter time than those on the left. This feature emphasizes the sensitivity of the temperature to the residence time in the electric field.

4.2. *Experimental results*

4.2.1. *Velocity and temperature fields.* To compare the numerical and experimental results, we measured axial velocity profiles for a flow rate fixed at 150 l h^{-1}, corresponding to a mean velocity of 5.21 mm s^{-1}. Velocity profiles are measured at three streamwise positions in the test section:

(1) at the entrance to the test section, which corresponds to 50 mm upstream of the electrode plates. This position is 190 mm downstream of the entry to the duct which precedes the test section; therefore, the flow is more or less fully developed.

(2) halfway from the upstream edge of the electrode plates. This position coincide with the horizontal slot of the H-shaped window in the electrode plate for flow visualization and velocity measurement. The distance between the beginning of the electrode plate and this measurement position is 150 mm.

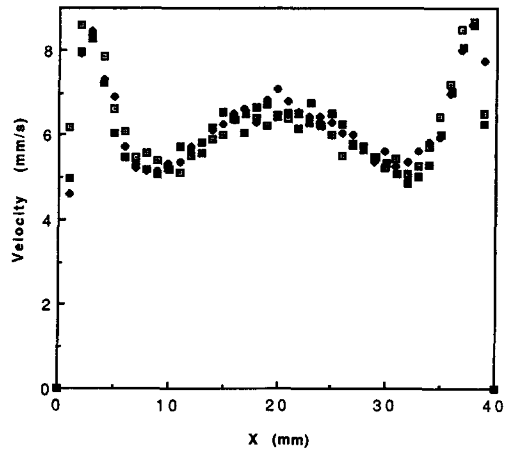

Fig. 10. Velocity profile in the middle of test section: experiment.

(3) at the exit from the test section, 4 mm upstream of the end of the electrode plates.

Figure 9 shows the velocity profile in the test section span at the entrance to the test section for two series of measurements for the same values of parameters to verify the scatter and reproducibility of the data.

Figure 10, superposing three velocity profiles measured in the middle of the electrode plates for the same thermal and flow input conditions, shows that the reproducibility is satisfactory. The significant feature in this profile is the considerable acceleration of the flow close to the electrode walls and its consequent deceleration in the center of the test section, as was observed in the numerical results (Fig. 3). The coupling between the thermal and hydrodynamic field is shown in Fig. 11, in which two velocity profiles measured at the mid-height of the test section are superposed. The profile measured in the presence of the electric field has a shape similar to the profile in Fig. 10. The other, measured for the same flow rate but without electric field, is parabolic. The same figure also shows the velocity profile measured at the entry

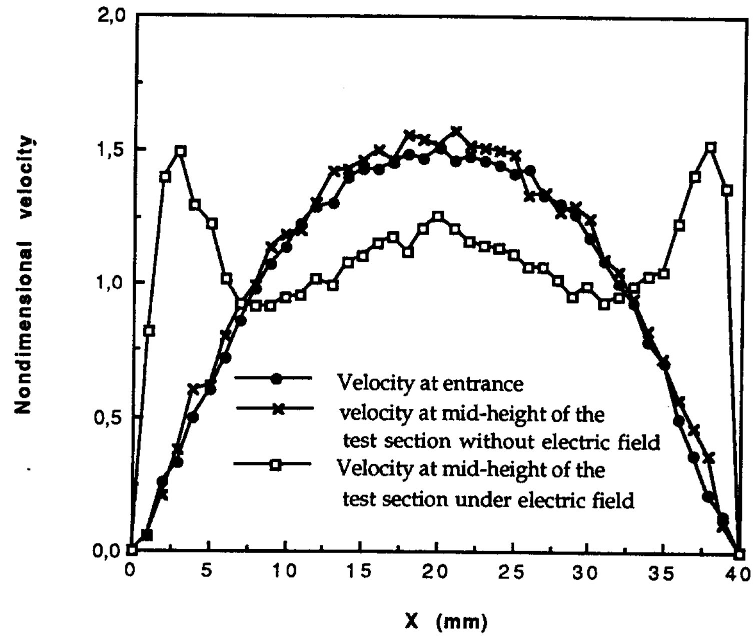

Fig. 11. Experimental velocity profiles in the middle of test section with and without applied electric field, compared with velocity profile at entrance.

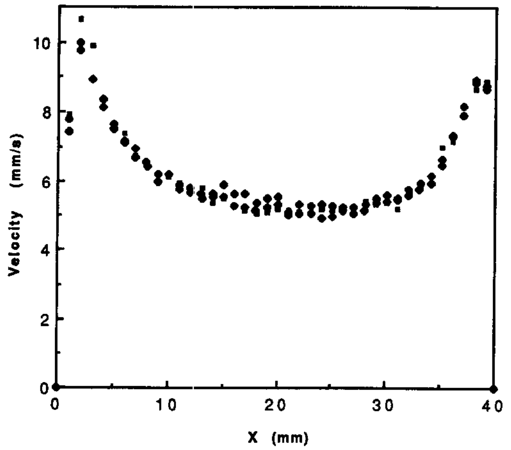

Fig. 12. Velocity profile at exit from test section.

of the test section, the similarity of the cold velocity profile in the middle of the test section and the velocity profile at the entrance is clear.

Figure 12, which gives the velocity profile at the exit of the test section for three series of similar flow parameters, shows a stronger effect of temperature field on velocity. The wall-region acceleration and consequent central-region deceleration are so strong in this profile that the velocity distribution in the duct span has changed dramatically; contrary to the entrance parabolic velocity profile, the velocity at the center is lower than on the walls. The strong sensitivity of the velocity profile to ohmic heating is also evident from the asymmetry of the velocity maximum on the left and right side of the velocity profile. We recall that a similar feature in the temperature profiles was explained by the unequal lengths of left and right electrode plates.

4.2.2. *Flow visualization.* The wall region is strongly affected by the high temperature gradient and electric body force. Complex phenomena can occur in the low-speed fluid layer adjacent to the electrodes. In order to study the flow on the electrodes, a flow visualization technique was used that allows characterization of the qualitative nature of the flow and more particularly of the instabilities generated by the applied electric field. We use the laser-induced fluorescence (LIF) visualization technique, the principle of which is explained in more detail in [12]. A fluorescein tracer is injected into the flow and flow cross-sections are illuminated by a laser sheet. The tracer partially absorbs the light at the wavelength contained in the laser sheet and emits light at a longer wavelength in all directions in space with equal probability. The emitted light is linearly proportional to the fluorescein concentration, which in turn is related to the flow structure.

The dye, which is stored in a small reservoir elevated above the test section, supplies a lower tank that distributes the dye to the different dye injection channels in the test section. The tracer flows through the porous metallic bar (Poral) under the hydrostatic pressure difference. In this manner the tracer is introduced on the test section wall with an almost zero normal to the wall velocity, and thus, it does not perturb the main flow.

A 5W argon ion laser delivers a narrow light beam that is transmitted to the test section via a fiber optic. A cylindrical lens converts the laser beam into a laser sheet that illuminates the flow through the H-shaped

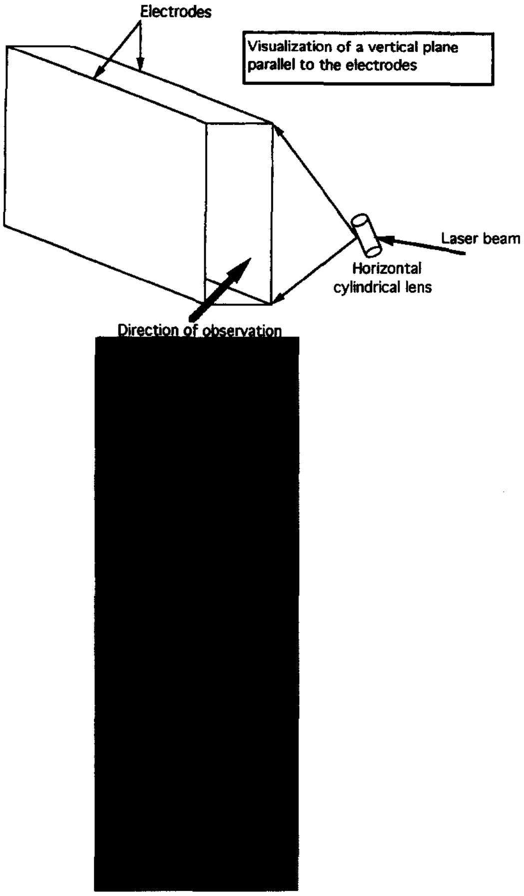

Fig. 13. Photograph of fluid layer adjacent to electrode, showing appearance of streaks under effect of electric field.

window in the electrode plates. The illuminated plane in the flow can then be viewed through the vertical side walls of the test section perpendicular to the electrode plates, and can be filmed by a CCD camera. Images are displayed on a monitor screen, recorded on videocassette, and later are analyzed with a digital-image-processing system.

Two types of flow visualization experiments were carried out: illumination of a flow plane perpendicular to the electrode plate and flow direction, and illumination of a fluid layer parallel and adjacent to the electrode plate (see Fig. 13).

In the cold flow, visualized by the first technique, we observe that dye injected on the wall stays close to it over the whole length of the test section, indicating that there is indeed a stable laminar flow. When the electric field is turned on, we observe vigorous mixing of the dye layer with the liquid in the test section during a transition period, which lasts a few tens of seconds. After the transition period, the dye layer is clearly diminished in the vicinity of the wall by a kind of suction that originates on the upper edge of the electrode and gradually reaches its lower edge. Certain zones of the flow, more or less regularly spread on the electrodes, show that the dye ejected away from the electrodes reaches the middle of the channel and mixes with the clear fluid. The dye suction event is attributed to the acceleration of the liquid layer in the vicinity of the wall within the heating zone. As the velocity profiles show, this acceleration is compensated by a deceleration of the fluid flowing in the middle of the test section.

In the second type of flow visualization experiment, we illuminated the flow in a plane parallel to the electrode plate and in contact with it. For the cold flow, a uniform sheet of dye covering the electrode is observed. However, for the hot flow under the effect of an electric field, organized structures in the form of very small parallel streaks, similar to Götler vortices in a concave boundary layer [12], are superposed on the dye film. We have verified the presence of these streaks by visualizing the dye-film cross-section with a laser sheet perpendicular to the flow direction. For the cold flow, the dye cross-section is uniform, with no evidence of streaking. However, when the electric field is turned on the streak cross-sections appear as dots in the visualization plane. Similar streaks have also been observed by Fujino and Mori [13] in a plane Poiseuille flow with a d.c. voltage difference applied on the electrode walls; the working fluid in their experiment was a strong electric insulator and one of the electrode plates was also electrically heated.

The striation can be viewed through the H-shaped window machined in the electrode. Figure 14(a) shows a number of the streaks as viewed from the vertical branch of H-shaped window and Fig. 14(b) shows the array as viewed from the horizontal branch of the window. Figure 15 plots the intensity distribution across the array of streaks in Fig. 14(a) vs the pixel number, from digital image processing; this figure shows a periodic distribution with maximum amplitude at the transverse locations where fluorescein concentration is maximum. The fast Fourier transform (FFT) of the waveform in Fig. 16 shows a frequency equal to 0.1, which corresponds to a wavelength $\lambda = 1.54$ mm. The wavelength is averaged over four streaks. However, the concentration distribution extracted from a larger number of streaks [as in Fig. 14(b)] has a less regular pattern, as shown in Fig. 17. The FFT analysis of this waveform in Fig. 18 gives a frequency equal to 0.07, corresponding to a physical wavelength $\lambda = 2.87$ mm. In fact, the discrepancy between the two wavelengths shows that the phenomenon is dominated by the upstream distribution of the perturbations. This situation has also been encountered in Görtler instability flow, where a constant wavelength has not been confirmed [14]. In this view, the flow is locally partitioned, in such a way that one pair of vortices can break down into turbulence at a streamwise location while a neighboring pair is still regular.

The generation and dynamics of the array of streaks needs more detailed investigation. Since the present experimental apparatus does not allow such detailed observation, an experimental apparatus with trans-

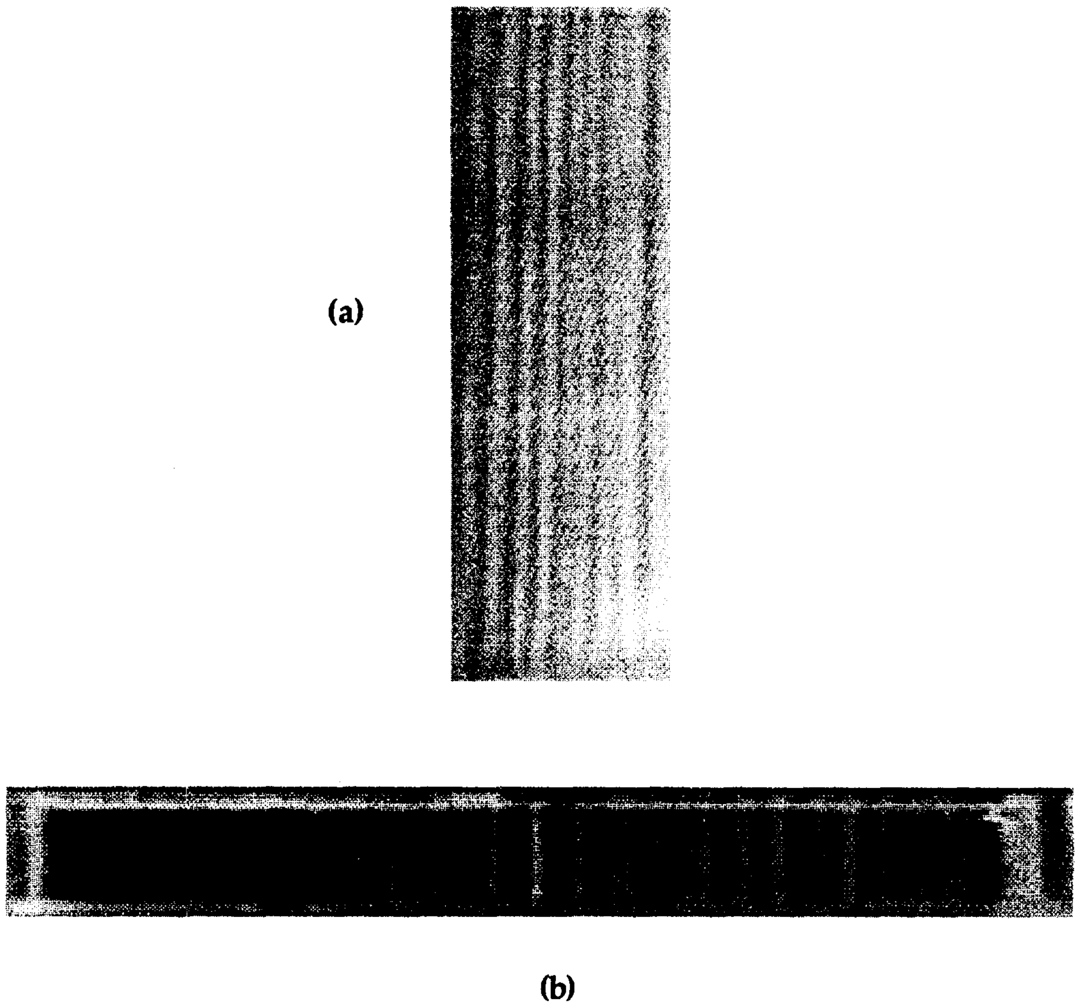

Fig. 14. (a) Photograph of streaks on electrodes viewed from vertical branch of H-shaped window. (b) Photograph of the streaks on electrodes viewed from horizontal branch of H-shaped window.

parent electrodes is under construction for this purpose.

4.2.3. *Origin of instability.* We have seen that when a flowing liquid is subjected to an electric field in the presence of a temperature gradient, an electric force $\vec{f}_e$ appears. Combining equations (4), (6), (7), (8) and (9) gives the following expression for this force:

$$\vec{f}_e = \left(\frac{\partial \varepsilon}{\partial T} - \tau_\sigma \frac{\partial \sigma}{\partial T}\right).(\vec{\nabla} T.\vec{E}).\vec{E}$$

so that $\vec{f}_e$ is thus proportional to and colinear with the electric field $\vec{E}$. In the present study the temperature gradient has two components: a vertical (streamwise) component linked to the change in the liquid temperature, from T_{in} to T_{out} as the liquid travels through the test section. The other component of the temperature gradient is horizontal and is caused by the difference in velocity between the channel center and the wall region. We thus have an electric force density that also has two components. However, since the electric field is uniform over most of the volume and the vertical component of the temperature gradient is perpendicular to the electric field, the electric force in this case has only one component that is horizontal (perpendicular to the electrodes). Given the orientation of the temperature gradient in our case, an approximate calculation shows that this electric force is oriented from the wall towards the liquid.

In the absence of main flow, a particle situated in the vicinity of the wall undergoes both the electric force $\vec{f}_e$ (horizontal) and the pressure force $\vec{P}$ (vertical). The resultant of the two forces, $\vec{R}$, is oriented obliquely from the wall to the liquid. This situation is analogous to an inclined Rayleigh–Bénard thermoconvective instability [15, 16]. In the latter configuration, the fluid particles are subjected to a buoyancy force directed vertically and therefore obliquely with respect to the wall. It is well known that in such a situation and under the action of thermoconvective forces, Rayleigh–Bénard rolls appear [15, 16]. This analogy can then explain the dye streaks, which, in our case, appear along the electrode under the effect of the electric field.

Additional experiments have let us determine the

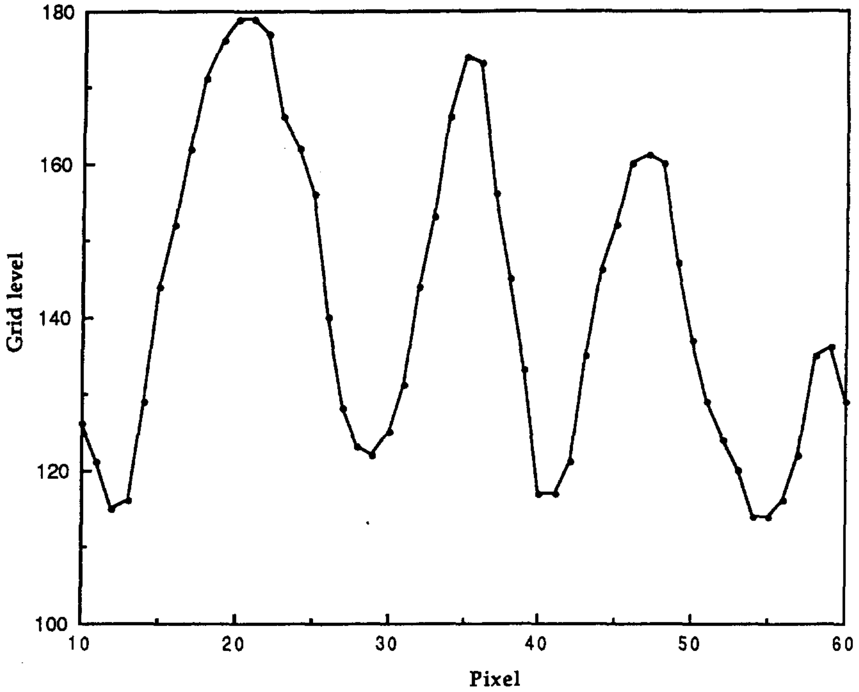

Fig. 15. Gray-level variation of streaks in Fig. 14(a).

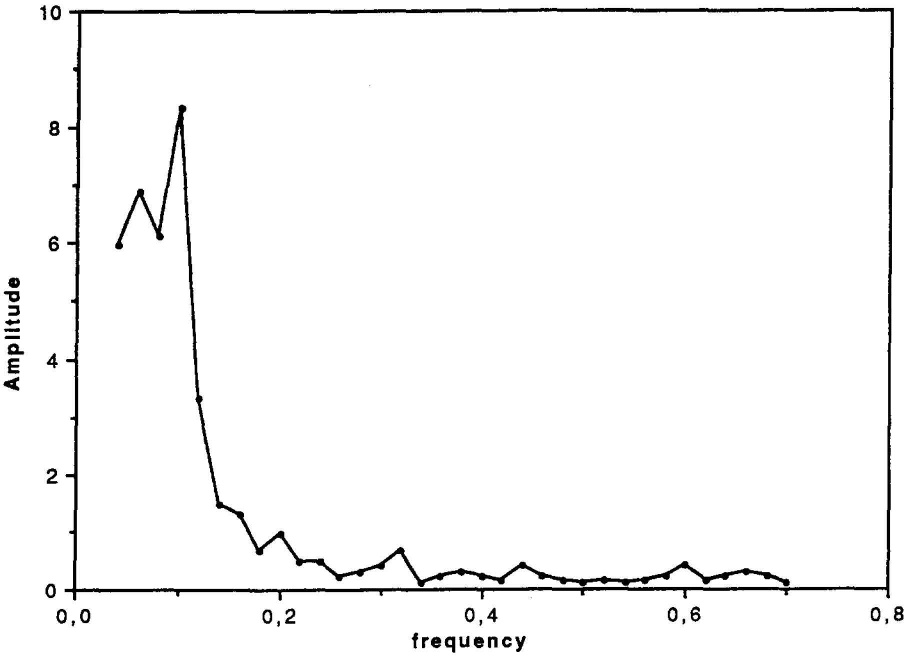

Fig. 16. Frequency spectrum of gray-level variation in Fig. 15.

critical values of the nondimensional numbers controlling the phenomenon:

Electrical Grashof number:

$$E_1'' = \left(\frac{\partial\varepsilon}{\partial T} - \tau_\sigma \frac{\partial\sigma}{\partial T}\right) \cdot \frac{\rho_0 E^2 \Delta T_{\text{ref}} l^2}{\mu_0^2}$$

Rayleigh number:

$$Ra = \frac{\beta g l^3 (T_{\text{out}} - T_{\text{in}})}{\nu_0 a_0}.$$

Preliminary results show that the longitudinal streaks appear for $E_1'' = 0.95$ and $Ra = 1.11 \times 10^5$ while a higher instability mode appears for $E_1'' = 1.3 \times 10^3$ and $Ra = 3.72 \times 10^6$. This mode corresponds to an oscillation of the steak which begins in the upper part of

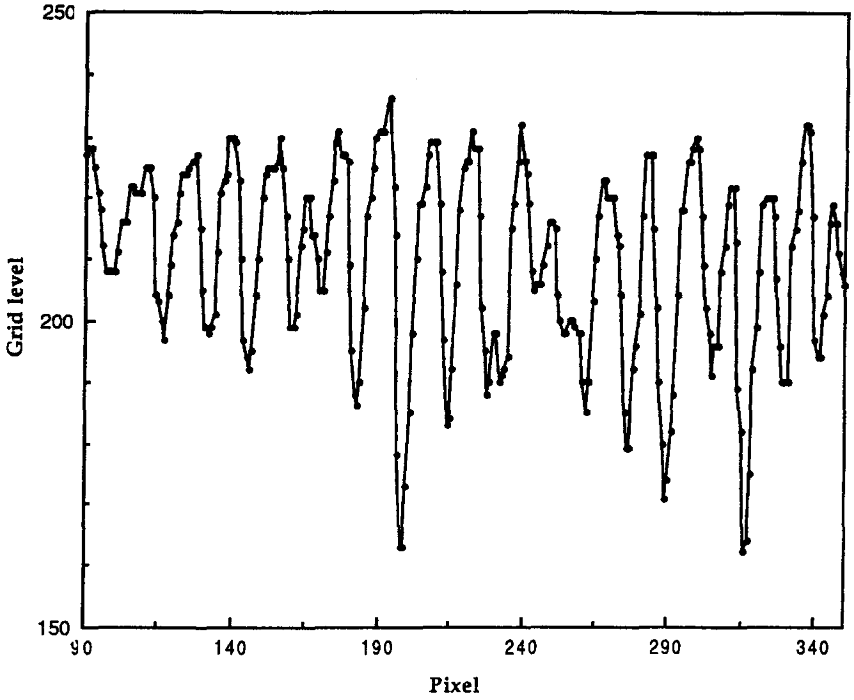

Fig. 17. Gray-level variation of streaks shown in Fig. 14(b).

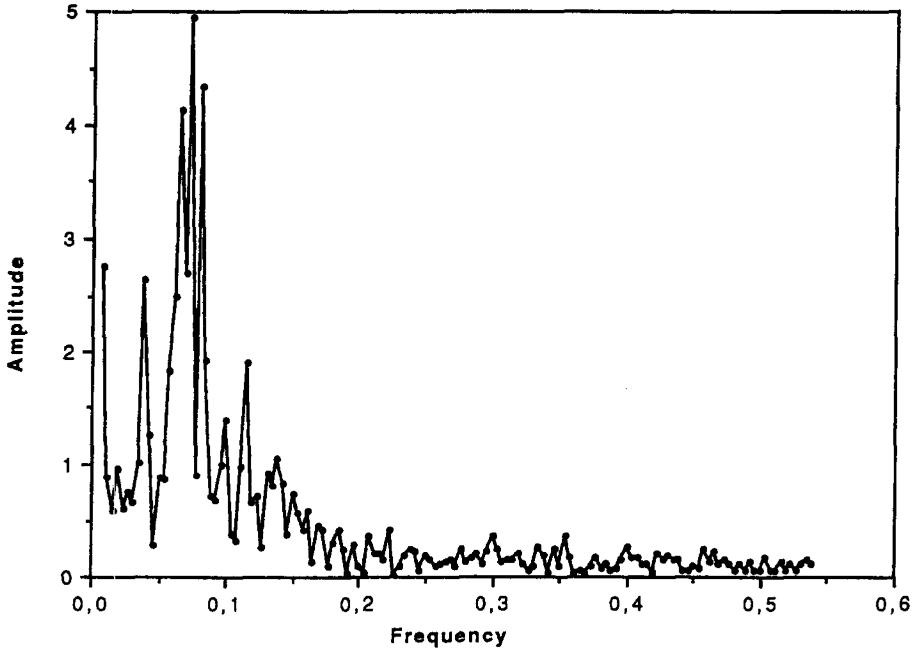

Fig. 18. Frequency spectrum of gray-level variation in Fig. 17.

the test section while the streaks begin to appear at the bottom end of the electrode. Oscillation of the vortices and interaction between neighboring vortices have been observed in Görtler instability [17], where they constitute the higher modes of instability before breakdown into turbulence. It should be emphasized that the experimental study for which the velocity and temperature profiles are given in Section 4.2 was carried out for $E_1'' = 1.46 \times 10^4$ and $Ra = 1.52 \times 10^7$, which corresponds to a situation beyond the point at which the higher mode of instability appears.

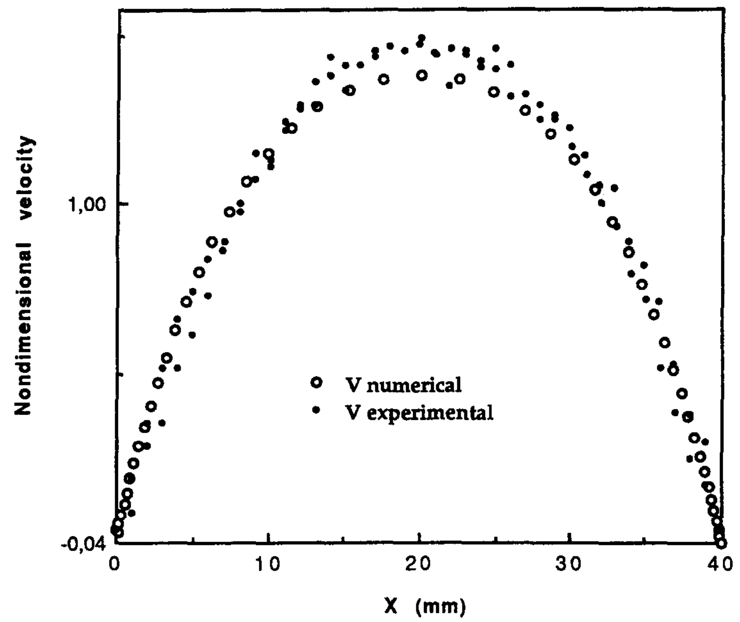

Fig. 19. Comparison of numerical and experimental velocity profiles at entrance to test section.

5. VALIDATION OF THE NUMERICAL MODEL

Comparisons are made for profiles measured at the key points in the test section. For the velocity profiles, the points are at the input to the test section, in the middle of the electrodes, and above the electrodes. For the temperature, we are limited by our instrumentation the profiles at the exit plane of the test section.

5.1. *Comparison of the velocity profiles*

Nondimensional numerical and experimental velocity profiles are compared. For the numerical data, the flow consists of a 2D laminar flow between two parallel plates with mean velocity 7.3 mm s^{-1}. The numerical values are nondimensionalized by this mean velocity. Experiments have been carried out with a mean velocity equal to 5.2 mm s^{-1}. The various profiles are measured in the median plane of the test section, they show, for cold flow, a mean velocity which is slightly higher, 5.65 mm s^{-1}. This mean velocity is obtained by integrating the velocity profile at the median plane of the test section. It is higher than the nominal mean velocity due to the flow acceleration in this plane. We use the latter velocity to nondimensionalize the experimental profiles. The experimental velocity profile measured at the entrance to the test section has been interpolated and used as the initial condition for the numerical solution of the governing equations. This profile is approximated with a polynomial of fifth degree with a correlation coefficient of 0.995.

Figure 19, which superposes this profile on other experimental velocity profiles measured at the same section, shows small differences (up to 0.7% in the middle of the curve) between the extrapolated experimental profile and the experimental profiles. These differences are of the same order as the measurement scatter at this point. Figure 20 superposes velocity profile obtained by numerical solution for the middle of the test section with some experimental velocity profiles measured at the same position within the test section. The curve has two distinct parts: a 'middle region' represented by the abscissa $5 < x < 35$, and a 'wall region' that corresponds to the rest of the span; $0 < x < 5$ and $35 < x < 40$. The middle region shows good agreement between numerical and experimental results; the maximum differences are around 8%, of the order of the scatter in the experimental values.

In the wall zone, however the difference between the experimental and numerical data is much larger, as much as 25%. The possible sources of errors that can yield this discrepancy are:

(1) measurement error in the velocity: to determine this error, we consider that the greatest source of error is introduced by the measurement of the interfringe distance. We assess this error as 2.6% and

(2) positioning error: an error in the positioning of the measurement volume, especially at the walls, can introduce a spatial shift that can yield hence a difference between the values measured at the same point in different experiments. We consider that position of the measurement volume with respect to the wall can be known within 2.5%.

The combination of these errors can explain the measurement scatter and therefore the difference between the experimental and numerical results in the middle region. However, in the wall region this combined error is still small in comparison to the difference between the experimental and numerical

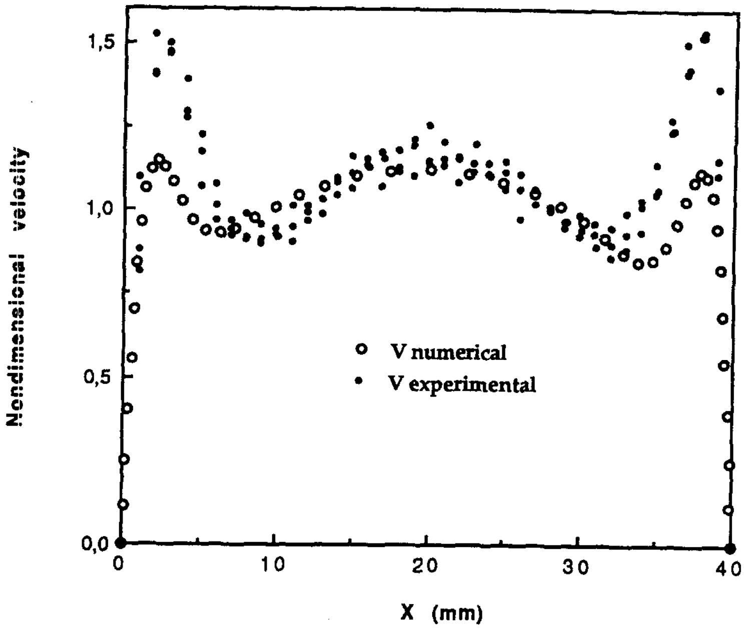

Fig. 20. Comparison of numerical and experimental velocity profiles in the middle of test section.

results. In this region, the acceleration of the fluid in the vicinity of the walls is much larger in the experimental data than in the numerical results. This difference can be attributed to three sources.

(a) We observed in the preceding section an increase in the average velocity in the heating case over that measured for cold flow, and attributed this increase to 3D effects caused by the application of the electric field. The same 3D effect could introduce a difference between the numerical and experimental data, since in the numerical model we assume a 'perfect' 2D flow.

(b) It was also observed that under certain conditions, an electric body force can cause the electroconvective instability phenomenon. The numerical results presented here are from the system of equations (14) where the electric force density was neglected. A possible contribution of this force could also explain in part the difference between the experimental and numerical curves, especially since this difference occurs where the temperature gradient is strongest and the electric force is indeed proportional to the temperature gradient.

(c) Another reason is the fact that the H-shaped slot machined in the electrode decreases the electrically active surface of the electrode and causes a current density concentration and therefore an additional overheating in the electrode. In the numerical model, however, the electrode is considered as continuous. The particles in the vicinity of the wall, warmer in fact than the numerical model predicts, are accelerated, whence the significant difference in the wall region.

(d) Strong velocity gradient close to the wall conjugated with the large measuring value size (0.9 mm) can also contribute to the discrepancy of the results close to the wall.

Figure 21 compares the numerical and experimental velocity profiles at the exit from the test section and shows good agreement between the different curves in the middle region, where the difference does not exceed 9%. However, a greater deviation is observed in the wall region, of about 18%. While the latter deviation is significant, it is smaller than what occurred previously at the mid-height of the electrodes and in the vicinity of the wall. This deviation can be attributed to the same phenomena as those in Fig. 20. However, the exit velocity profiles shown in Fig. 21 are situated above the heating zone, which explains the relative attenuation of the acceleration in the wall region and therefore the smaller difference between the numerical and experimental results.

5.2. *Comparison of the temperature profiles*

We use dimensionless temperatures to compare the numerical and experimental temperature profiles. In the computations, T_{in} is the temperature boundary condition at the input to the geometry and T_{out} is the average temperature calculated from the test-section exit profile. In the experiments, T_{in} and T_{out} are the temperatures indicated by the thermocouples at the inlet and exit of the apparatus far upstream and downstream of the test section and they are therefore the average temperatures. In both numerical and experimental cases, the average temperature increase of the fluid between input and output is 10.5 K.

Figure 22 shows the numerical and experimental nondimensional temperature profiles at the exit from the test section, 4 mm above the upper end of the electrodes. We see good agreement between the exper-

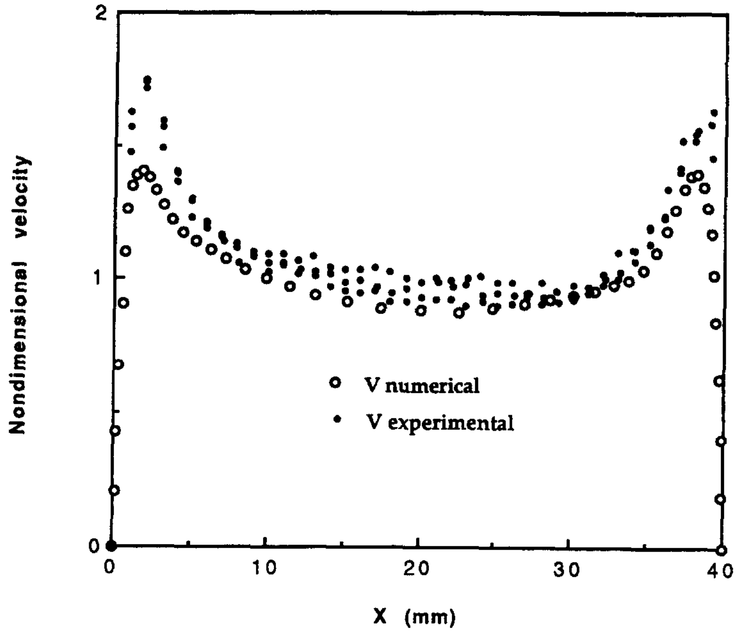

Fig. 21. Comparison of numerical and experimental velocity profiles at the exit from test section.

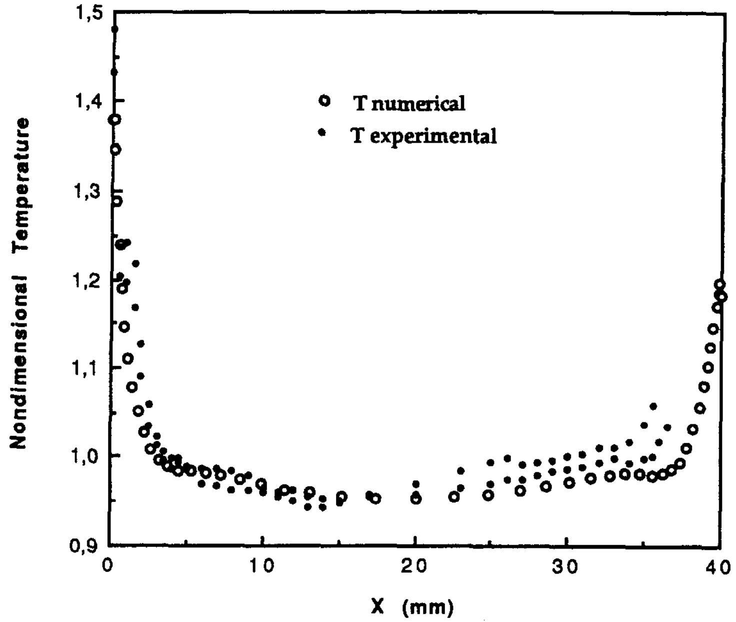

Fig. 22. Comparison of experimental and numerical temperature profiles at upper edge of electrodes.

imental and numerical curves, with a difference at the wall of 7% that is larger than that in the middle (0.15%). This larger difference tends to confirm the hypothesis of overheating due to current density concentration that was advanced above to explain the difference between the velocities at this point.

6. CONCLUSION

The general system of equations governing direct electric conduction was established. It was used to analyze the interactions between the various physical phenomena involved: hydrodynamic, thermal and electric phenomena. The analysis was performed for the particular case of an ionic liquid flowing in a 2D geometry. It was shown that in addition to the natural convection, a regime of electroconvection can occur in certain cases. By using the code ULYSSE and a new subprogram developed here, the system of equations corresponding to the simplified case of a 2D channel flow and negligible electric force was resolved. The resolution of even such a simplified system remains complex because of the nonlinearities and couplings among the various physical phenomena involved.

In principle, the numerical results allow an improved understanding of the local phenomena and help to interpret tests on industrial equipment of this type. The numerical model developed here proved useful in the design and optimization of future ohmic heaters. However, before we could use the numerical results systematically, they had to be validated by comparison to the experimental results. The comparison of the numerical and experimental results shows in general a fairly good agreement in the mid span of the test section but significant difference in the vicinity of the electrodes. This suggests examining the rate of the volume electric force as a source for this difference. In addition, thermally isolated boundary conditions on the electrodes should be relaxed in the computations. In spite of the differences between the experimental and numerical results, the numerical model describes quite well the evolution of the velocity and temperature fields as the fluid flows in the system.

Experiments showed longitudinal streaks appearing on the electrodes that can be attributed to an instability mechanism similar to Rayleigh–Bénard instability. The driving force here is the electric body force. The wavelength of the streaks is not regular in the span, but varies between 1.54 and 2.87 mm. The electroconvective instabilities are of particular interest in that they allow reorganization and meandering of the hydrodynamic and thermal boundary layers and therefore equalization of heat flux and temperature distribution on the wall.

REFERENCES

1. A. A. P. De Alwis, K. Halden, and P. J. Fryer, Shape and conductivity effects in the Ohmic heating of foods, *Chem. Engng Res. Des.* **67,** 159–192 (1989).
2. C. H. Biss, S. A. Coombes and P. J. Skudder, The development and applications of ohmic heating for the continuous processing of particulate foodstuffs. In *Process Engineering in the Food Industry* (Edited by R. W. Field and J. A. Howell). Elsevier, London (1989).
3. T. B. Jones, Electrohydrodynamycally enhanced heat transfer in liquids—A review, *Adv. Heat Transfer* **14,** 107–148 (1978).
4. H. Senftleben and W. Braun, Der Einfluss elektrischer Felder auf den Wärmestrom in Gasen, *Z. Phys.* **102,** 480–500 (1936).
5. R. J. Turnbull, Effect of a non-uniform alternating electric field on the thermal boundary layer near a heated vertical plate, *J. Fluid Mech.* **49,** 693–703 (1971).
6. R. Durand and J. J. Rameau, Chauffage ionique d'une émulsion de latex. Final report on collaboration between EDF and INPG-CNRS (contract 3-L-8478), Grenoble (1989).
7. A. Ould El Moctar, H. Peerhossaini, P. Le Peurian and J. P. Bardon, Ohmic heating of complex fluids, *Int. J. Heat Mass Transfer* **36**(12), 3143–3152 (1993).
8. R. Kronig and G. Ahsmann, The influence of an electric field on the convective heat transfer in liquids, *Appl. Sci. Res. A* **2,** 31–32 (1949).
9. E. Bonjour and J. Verdier, Interprétation de l'action de champs électriques sur les transferts de chaleur dans les liquides diélectriques. *C. R. Hebd. Séances Acad. Sci.* (Paris) **250,** 998–1000 (1960).
10. D. Laurence, Code ULYSSE: Notice de Principe, Rapport EDF HE 41/89-32B (1989).
11. A. Ould El Moctar, *Etude des phénomènes physiques couplés lors du chauffage volumique d'un liquide ionique en écoulement par conduction électrique directe,* Thèse de Doctorat, Université de Nantes–Ecole Centrale de Nantes (1992).
12. H. Peerhossaini and J. E. Wesfreid, On the inner structure of streamwise Görtler roles, *Int. J. Heat Fluid Flow* **9,** 12–18 (1988).
13. T. Fujino and Y. H. Mori, The effect of transverse electric field on laminar Channel flow with a constant heat rate. In *Flow Visualisation IV* (Edited by C. Veret), pp. 643–648. Hemisphere, Washington, DC (1987).
14. J. D. Swearingen and R. F. Blackwelder, The growth and breakdown of streamwise vortices in the presence of wall, *J. Fluid Mech.* **182,** 255–290 (1987).
15. J. E. Hart, Stability of the flow in a differentially heated inclined box, *J. Fluid Mech.* **47** 547–576 (1971).
16. R. J. Goldstein and Q. J. Wang, An interferometric study of the natural convection in an inclined water layer, *Int. J. Heat Mass Transfer* **27,** 1445–1453 (1984).
17. H. Peerhossaini and J. E. Wesfreid, Experimental study of the Taylor–Görtler instability. In *Propagation in Systems far from Equilibrium* (Edited J. E. Wesfreid, H. R. Brand, P. Manneville, G. Albinet and M. Boccara). Springer, Berlin (1988).